RSC Advances

ROYAL SOCIETY OF CHEMISTRY

www.rsc.org/advances

Biomimicking structure of silk fibers *via* cellulose nanocrystal as β-sheet crystallite

Lin Liu[1,2], Xiaogang Yang[1], Houyong Yu[1,2], Chao Ma[1] and Juming Yao[1,2*]

[1]*The Key Laboratory of Advanced Textile Materials and Manufacturing Technology of Ministry of Education, College of Materials and Textiles, Zhejiang Sci-Tech University, Hangzhou 310018, China*

[2]*National Engineering Lab of Textile Fiber Materials & Processing Technology, China*

*Corresponding author: College of Materials and Textile, Zhejiang Sci-Tech University, Xiasha Higher Education Park, Hangzhou 310018, China

Tel: +86-571-86843251 Fax: +86-571-86843619

Email: yaoj@zstu.edu.cn

Abstract

Inspired by such an ordered *β*-sheet crystalline structure and molecular orientation of natural silkworm silk, biomimic silk fibers with refined crystalline structure were creatively produced through incorporating cellulose nanocrystals (CNCs) into silk fibroin (SF) matrix to mimic the *β*-sheet crystallites in natural silk *via* wet-spinning assembly technology in this paper. The influence of CNCs and post-draw on the structural characteristics, thermal and mechanical properties of regenerated cellulose nanocrystal/silk fibroin (CNC/SF) fibers were comparatively studied with those of degummed silk. The resultant CNC/SF fibers exhibited a uniform, circular shape as well as dense morphology. The CNCs were uniformly dispersed into SF matrix and aligned along the fiber axis, which were beneficial to the formation of more ordered structure through intermolecular hydrogen bonding interactions. The crystallinity and overall molecular orientation of CNC/SF fibers were increased with increases of draw ratio and CNC contents, although lower than those of degummed silk. DSC and TGA analysis revealed that thermal decomposition behavior of CNC/SF fibers presented different features depending on the CNC contents, whereas maximum decomposition temperature of CNC/SF fibers improved sharply at first and then decreased slightly with the increase of CNC contents. Moreover, the tanδ peak temperatures of SF were increased with the addition of CNC, indicating restrained SF molecular mobility in the vicinity of the CNC surface. These results indicated that the CNC could substantially enhance the mechanical properties of SF and this enhancement could be attributed to the strong hydrogen bonding interactions as well as CNC-induced

crystallization and orientation. Meanwhile, Young's modulus, tensile strength and breaking strain of the CNC/SF fibers with 5 wt% CNC were significantly increased to 28.8±2.6 GPa, 728.5±36.4 MPa and 23.1±1.6% respectively, higher than those of degummed silk. Thus it was demonstrated that biomimicking the natural silk crystalline structure using CNC as *β*-sheet crystallite is a promising strategy for production of artificial silk fiber with improved strength without compromising the toughness.

Keywords

Silk fibroin; Cellulose nanocrystal; Biomimicking structure; Crystalline structure; Orientation; Mechanical property

Highlights

Biomimic silk fibers with refined crystalline structure were creatively produced *via* incorporating cellulose nanocrystals into silk fibroin matrix to mimic the *β*-sheet crystallites in natural silk. The resultant fibers exhibit excellent thermal and mechanical properties, which are attributed to the strong hydrogen bonding interactions between cellulose nanocrystals and silk fibroin as well as cellulose nanocrystal-induced ordered structure.

1. Introduction

Nature has created amazing materials during the process of evolution, inspiring scientists and engineers to tirelessly mimic them. Silkworm silk, produced by *Bombyx mori*, is of particular interest, and it has been researched for more than fifty years for its various applications in not only textile, but also optical and biomedical fields owing to its comprehensive mechanical properties.[1-8] Each silk fibers is about 10-25 μm wide and contains two different proteins, the core structural protein called fibroin and the gummy sheath protein called sericin.[9,10] The main structural protein, fibroin is dominated by the highly repetitive structural modifs GAGAGS, forming well-ordered *β*-sheet crystallites interspersing among the less ordered noncrystalline regions of the protein matrix.[11-15] The formation of hydrogen bonding network between these *β*-sheet crystallites plays a key role in defining the strength and rigidity of this material, while the noncrystalline regions adopting much more flexible conformations contribute to elasticity. [9,10] In a sense, natural silk fiber can be considered a complexes reinforced by *β*-sheet nano-crystallites.

To produce engineered silk fiber with excellent mechanical properties, diverse artificial spinning methods, such as wet-spinning, electrospinning, and microfluidic approaches, have been developed. For example, regenerated silk fibroin (SF) fibers were prepared using wet-spinning from 1,1,1,3,3,3-hexafluoro-2-propanol (HFIP),[16] hexafluoroacetone (HFA),[17] trifluoro-acetic acid (TFA),[18] formic acid,[19] *N*-methyl morpholine *N*-oxide (NMMO),[20] ionic liquid[21] and aqueous solution,[22-24] usually into methanol bath. Electrospinning was employed to produce regenerated SF fiber in

form of nano-films used as scaffolds for biomedical applications.[25-29] A microfluidic chip was used for the concentration of regenerated SF aqueous solution to mimic the silk glands and the spinning duct of silkworms.[30-33] However, resultant SF fibers described above were lower strength and weaker properties than their natural counterparts, with the exception of Ha's [18] and Zhou's.[22] Ha *et al*. dissolved SF in TFA, causing this method unsuitable for industrialization. The procedure of Zhou *et al*. produced stronger regenerated SF fibers compared to degummed cocoon silk using SF aqueous solution, but it performed a high drawing (6X) which caused the fibers brittle in the processing stage.

It's well known that silk fibroin is synthesized at the epithelial wall of the posterior silk gland. The fibroins subsequently are secreted into the lumen as an aqueous solution of 12-15 wt% and extruded to the middle division, where the concentration of fibroin increases. In anterior division, the concentration of fibroin further increases to about 30 wt%, finally fibroins are spun into water-insoluble fiber by mechanical shear and stretching of the spinneret. Simultaneously, the fibroins undergo the conformational transition from a random coil to well-oriented β-sheet crystalline structure. [9,10,34] Briefly, the spinning process of silkworm as shown in Fig. 1a, involves a liquid crystal spinning process. Shearing and stretching orients the fibroin molecule chain, and the liquid is converted into fibers. The formation of oriented β-sheet crystallites by means of hydrogen bonds and the configuration of molecules by solvent exposure are crucial to the mechanical properties of *B. mori* silk.[9,10,35-37]

Inspired by such well-ordered β-sheet crystalline structure as well as molecular

orientation, forming the basis for the mechanical strength of silk fiber in the silkworm spinning mechanism, a series of ordered crystallization, well orientation, regenerated cellulose nanocrystal/silk fibroin (CNC/SF) fibers were firstly fabricated by wet spinning using water/methanol system. Creatively, we introduce cellulose nanocrystals (from waste mulberry branch bark) to mimic the β-sheet crystallites in natural silk *via* hydrogen bonding interactions between carbonyl groups of SF and hydroxyl groups of CNC to govern the molecular structures and mechanical properties of regenerated CNC/SF fibers (as shown in Fig. 1b). It has been confirmed that CNCs possessed remarkable reinforcing effect due to its large aspect ratio, outstanding mechanical property (140-150 GPa of Young's modulus and 7 GPa of tensile strength), and high surface reactivity.[38-43] Thus it will be presumptive that having mimicking microstructure, strong and extensible CNC/SF fibers could be obtained in this work. In addition, the morphological feature, crystalline structure, molecular orientation, thermal and mechanical properties of CNC/SF fibers were comparatively studied with those of degummed silk.

2. Experimental section

2.1 Materials

B. mori silkworm cocoons, mulberry branch barks (*M. alba* L.) were obtained from Huzhou Academy of Agricultural Science (Huzhou, China). LiBr, methanol, polyethylene glycol (PEG) and other reagents used here were analytical grade and purchased from Hangzhou Mike Chemical Agents Co. Ltd., China.

2.2 Preparation of spinning dope

Colloidal solution of CNC was prepared from mulberry branch bark by the alkali treatment, followed by the sulfuric acid hydrolysis as described previously.[44] *B. mori* cocoons were degummed twice with 0.5% (w/v) Marseilles soap solution and washed thoroughly with distilled water to remove sericin. The degummed fibers were dissolved in 9.0 M LiBr solution at 37 °C for 2 h, filtered to obtain the SF-salt solution. The blend solution was prepared by mixing SF-salt solution with CNC colloidal solution in the following mass ratio: 99/1, 97/3, 95/5 and 93/7 (SF/CNC) under mildly stirring for 30 min at room temperature. Then the mixture was concentrated by reverse dialysis against 10% (w/v) of PEG solution at 4 °C to yield spinning dope with concentration of 27 wt%.

2.3 Preparation of cellulose nanocrystal/silk fibroin fibers

Regenerated CNC/SF fibers were produced using a custom-made industrial wet-spinning device at room temperature (Fig. 1b). The CNC/SF spinning dope was carefully transferred to the storage cylinder. A nitrogen pressure of 0.15 MPa controlled by a pressure regulator was used to extrude the spinning dope through a spinneret with 0.3 mm in diameter at a rate of 1.0 mL/min into a methanol coagulation solution at room temperature. The post-draw was performed under 60 °C, and the drawn ratio was defined as the rate ratio of the second roller to the previous one. The resulting fibers were further washed with water and then dried at 40 °C. Then CNC/SF fibers containing various content of CNC were prepared.

2.4 Characterization

The surface and the cross-section morphologies of CNC/SF fibers were observed

using SEM (JSM-5610, JEOL, Japan) and FESEM (S4800, Hitachi, Japan) after sputtering with gold. The cross-section of the fibers was obtained by fracturing them perpendicular to the fiber axis under liquid nitrogen. The diameters of the CNC/SF fibers were calculated from the sectioned fibers using the software provided with the SEM. The morphologies of CNC were also characterized using AFM (XE-100E, PSIA, Korea) and TEM (JEM-1230, JEOL, Japan) by dispersing diluted CNC suspension (0.1 wt%) on the surface of a clean silicon slice and carbon-coated copper grid, respectively, and dried at ambient temperature.

The intermolecular hydrogen bonding interactions between CNC and SF were characterized using ATR-FTIR spectrometry (Nicolet 5700, Thermo Electron Corp., USA) ranging from 4000 to 600 cm^{-1} with a resolution of 4 cm^{-1} and 16 scans. Data analysis was carried out by the OMNIC professional software.

The crystalline nature of CNC/SF fibers were evaluated with an X-ray powder diffractometer (XRD, ARL X'TRA, Thermo Electron Corp.) using a monochromatic CuKα radiation at λ=1.54056 Å in the range of 2θ = 5º-50º with a scanning rate of 3.0º min^{-1} and a step size of 0.04º. The crystallinity was taken as the ratio of the sum of areas under the crystalline diffraction peaks to the total area under the curve between 2θ = 5º and 50º.[45,46] The overall molecular orientation of CNC/SF fibers were determined quantitatively by SCY-□ sound velocimeter (Shanghai Kelly Chemical Fiber Co. Ltd., China).

The thermal decomposition behavior of CNC/SF fibers was conducted on a differential scanning calorimetry (DSC, TA- 2910, USA) and thermogravimetric

analyzer (TGA, Pyris Diamond I, Perkin-Elmer Corp.) with a heating rate of 10 °C/min in a nitrogen environment. Main thermal parameters were obtained from DSC and TGA curves, such as main endothermic peaks and maximum decomposition temperature (T_{max}), respectively.

The dynamic mechanical analysis (DMA) was performed on a dynamic thermal mechanical analyzer (Q-800, TA Instruments, USA) in tension mode. The samples were analyzed in single-cantilever mode at frequency of 1 Hz, at the temperature ranging from 50 °C to 250 °C with a heating rate of 5 °C/min in air atmosphere. The temperature corresponding to the peak in the loss tangent (tan δ_{max}) versus temperature plot was taken as the glass transition temperature (Tg).

The mechanical properties of CNC/SF fibers were measured on tensile testing equipment (XL-2, China) at 25±0.5 °C and 65±5% RH after the equilibration at above conditions for at least 24 h. The extension rate was 10 mm/min with a span of 5 cm, and the data reported were the average of 10 measurements.

3. Results and discussion

3.1 Morphological feature

In our previous work,[47] we have demonstrated a good spinnability of the CNC/SF dope solution with 27 wt% of high concentration. For deeply studying, here we designed and accomplished a biomimetic approach for the formation of regenerated CNC/SF fibers. Fig.2 showed the morphological features of CNC/SF fibers with 0, 1, 3, 5 and 7 wt% CNC, respectively. As a representative, the wet-spun regenerated fibers with 7wt% CNC exhibited a uniform, circular shape as well as dense

morphology, as shown in Fig. 2a. The diameter of the resultant fiber was significantly reduced as low as 53 μm after 3X of post-draw. Moreover, it was demonstrated that CNCs were uniformly dispersed in SF matrix by FESEM fractured morphologies. As shown by Fig. S1, the CNCs prepared from mulberry branch bark by sulfuric acid hydrolysis exhibited rod-shaped morphology with a diameter of 20 nm and a length of 300-400 nm. Once the CNCs were added into polymer matrix, the CNCs as "bright dots" in gray areas for SF matrix, were easily identified, and those "bright dots" were gradually increased with the increase of CNC contents in the CNC/SF fibers. A uniform distribution of CNCs in the SF matrix could be observed in all CNC/SF fibers, and it was also found that all CNC ends presented in the fractured surface, revealing these nanocrystals were aligned along the fiber axis.

3.2 Intermolecular hydrogen bonding interaction

Fig. 3 showed the FTIR spectra of degummed silk and CNC/SF fibers (3X) with various CNC contents. As to protein materials, characteristic vibrational bands in FTIR spectra indicate their conformations: 1660 cm^{-1} (random coil) and 1630 cm^{-1} (β-sheet) for amide Ⅰ, 1540 cm^{-1} (random coil) and 1520 cm^{-1} (β-sheet) for amide Ⅱ, and 1230 cm^{-1} (random coil) and 1270 cm^{-1} (β-sheet) for amide □.[15,18] The shift of these bands is attribute to the distinct hydrogen bonding states resulting from different conformations adopted by the molecular chains. It was found that all CNC/SF fibers exhibited typical β-sheet and random coil structure, similar with those of degummed silk although exhibiting broader bands. With the increase of CNC contents, a new peak at 1109 cm^{-1} assigned to C-OH association appeared in the CNC/SF fibers, and

the characteristic peak at 1062 cm^{-1} both in degummed silk and regenerated SF fiber gradually became sharp, as well as splited into two peaks at 1058 cm^{-1} and 1035 cm^{-1} corresponding to C-O skeletal vibration, indicating the presence of CNC in CNC/SF fibers (also supported by Fig. S2a). In addition, the characteristic vibrational bands for amide Ⅰ and amide Ⅱ gradually became narrow and shifted to low wavenumber with the increase of CNC contents (Fig. 3a), which indicated that more ordered structure caused by the incorporation of CNC might occur.

In this work, we mainly focused on the amide Ⅰ region (C=O stretching) to determine structure change, especial the intermolecular hydrogen bonding interaction between CNC and SF. As shown in Fig. 3a, the band at around 1629 cm^{-1} could be assigned to the hydrogen bonded C=O groups, and 1705 cm^{-1} to free C=O groups. The hydrogen bond fraction ($F_{H\text{-}CO}$) can be measured by the curve-fitting of the carbonyl band with Gauss/Lorentz spectral function. With the increase of the CNC contents, red shift (from 1705 cm^{-1} to 1699 cm^{-1}) in the band position for free C=O component occurred, whereas that for hydrogen bond component was almost unchanged, indicating the total area of the carbonyl bands becomes smaller as the CNC contents increased. In consideration of no absorption band of the CNC appeared in this region, any change here should be directly attributed to changes in the carbonyl group environments of SF, such as formation of new hydrogen bonds. The $F_{H\text{-}CO}$ values can be calculated to further estimate the amount of formed hydrogen bonding interaction in the CNC/SF fibers, and determined by the following equation[48,49]:

$$F_{H-CO} = \frac{A_H / r_{H/a}}{A_H / r_{H/a} + A_a} = \frac{A_H}{A_H + r_{H/a} A_a}$$

Where, A_H and A_a are the peak areas of hydrogen bond and free component, respectively, and $r_{H/a}$ is the specific absorption ratio of the above two bands. Fig. 3b showed a case, i.e. the curve-fitting of the carbonyl band with Gauss/Lorentz spectral function for CNC/SF with 7 wt% of CNC, and $F_{H\text{-}CO}$ values as a function of the CNC contents listed in Table 1. It was observed that with the increase of the CNC contens, $F_{H\text{-}CO}$ increased from 0.50 for the CNC/SF fibers with 1 wt% CNC to a maximum value of 0.60 for 7 wt%. From above, it was clearly confirmed that strong intermolecular hydrogen bonding interaction between CNC and SF matrix formed, consequently the molecular structures of CNC/SF fibers were further ordered.[43,49]

3.3 Crystalline nature and molecular orientation

In order to determine the crystalline characteristic and molecular orientation of the CNC/SF fibers, X-ray diffraction and Sonic orientation were performed. Fig. 4a showed the XRD patterns of degummed silk and regenerated SF fiber with different draw ratios, defined Di (i=1, 2, 3) for distinction. Regardless of the draw ratios, all regenerated SF fibers showed a broad shoulder at $2\theta=9.5^{\circ}$ and a main overlapped peak at $2\theta=19.4^{\circ}$ and 20.5°, respectively, which were attributed to a regular arrangement of interchains and intersheets in the β-sheet crystallites.[18,46] However, as-spun SF fiber exhibited a weak peak at $2\theta=24.5^{\circ}$, indicating the presence of a different type of crystalline structure for silk Ⅰ,[10,18] whereas the post-draw SF fibers showed a broad shoulder. The appearance and intensity of the crystalline peak at $2\theta=24.5^{\circ}$ revealed that the regenerated SF fibers possessed lower crystallization than degummed silk, and had a crystalline structure change from silk Ⅰ to silk Ⅱ in post-draw process,

which consisted with previous reports by Suzuki et al[11] and Ha et al[18]. Moreover, Fig. 4b showed the crystallinity of the regenerated SF fibers obtained by deconvolution of diffractograms in Fig. 4a. It could be seen that the post-draw SF fibers showed higher crystallinity than that of the as-spun fiber, although lower than that of degummed silk. However, the crystallinity has no obvious change with the increase of draw ratio from 1X to 3X, which is an indication that the post-draw of the SF fibers did not cause further crystallization. In our wet spinning process, the concentrated silk fibroin molecules (27 wt% of SF aqueous solution) were pre-crystallized simultaneously by methanol during the coagulation process. After post-draw, this less developed crystalline structure was improved (from silk Ⅰ to silk Ⅱ structure), consequently increasing the crystallinity. But further crystallization of the SF fiber (1X) will become difficult due to the suppression of a pre-crystallized region, which leads to no obvious change in crystallinity.

In the other hand, the effects of CNC on crystalline structure of CNC/SF fibers (3X) were studied. The XRD patterns and crystallinities of these fibers were shown in Fig. 5. It was found that all the CNC/SF fibers exhibited a typical β-sheet crystalline structure. With the increase of the CNC contents, the position of the (020) diffraction slightly shifted to higher angles (Fig. 5a), which illustrated the structure change of SF crystalline occurred because of the formation of defective SF crystals in the presence of CNC. Similar phenomenon was reported in CNC-reinforced composites.[38,40,49] In addition, a main crystalline peak at $2\theta=22.7^{\circ}$ ((200) lattice plane) appeared and strengthened with the increase of CNC contents, which was assigned to the cellulose I

structure of CNC (supported by Fig. S2b). It was also found that the position of the (200) diffraction gradually shifted to higher angles with the increase of CNC contents, which also reconfirmed the formation of interaction between SF and CNC in crystalline region. From Fig. 5b, it could be seen that the crystallinity of the CNC/SF fibers improved slowly at first and then increased obviously as CNC contents increased from 1% to 7%. Compared with pure SF fiber of 35.1%, the crystallinity of the CNC/SF fiber with 7 wt% CNC was increased to a maximum value of 53.7%, and larger than that of degummed silk of 44.5%. In our wet spinning process, methanol could induce the formation of a β-sheet structure from random coil/α-helix in SF. Moreover, the CNC could act as a nucleating agent to increase the nucleation and overall crystallization rate, leading to more perfect SF crystalline. Simultaneously, the strong intermolecular interaction between CNC and SF modulated the crystalline structure of SF matrix.

Sound velocity method is useful to explore the whole molecular orientation of fibrous materials.[50,51] Fig. 6 showed the velocity values of CNC/SF fibers with different draw ratio. An increase of sound velocity was observed for all CNC/SF fibers with the increase of the draw ratio, which indicated that the degree of molecular orientation along the fiber axis increased, although much lower than that of degummed silk of 16.8 km/s. However, compared with the pure SF fiber under constant draw ratio, the sound velocity of CNC/SF fibers decreased slightly with the increase of CNC contents and then increased when the CNC content increased to 7 wt%. This result might relate to the intermolecular interaction between CNC and SF.

Once the CNC added into the SF solution, the strong intermolecular interactions formed which restrained the stretch of the SF chains and subsequently resulting in the decrease of orientation. But during the drawing process, the SF molecular chains were extensively stretched, especially in the less developed crystalline regions and amorphous regions. Therefore, the sound velocity of the fibers exhibited an increase with draw ratio increasing. When the CNC content was increased to 7 wt%, this rigid nanocrystal oriented the molecular chains and aligned along the fiber axis. And the sound velocity even exceeded that of the pure SF fiber regardless of draw ratio. Since the sound velocity corresponds to the orientation of the total molecular chains, including crystalline orientation and amorphous orientation, it could be supposed that the intermolecular interactions occurred between CNC and SF in noncrystalline region of SF chains, and subsequently CNC arranged along the fiber axis under post-draw.

3.4 Thermal behavior

Thermal analysis was performed using DSC and TGA techniques to investigate the structural and thermal characteristics of degummed silk and various CNC/SF fibers (3X). As shown in Fig. 7 and Table1, regenerated SF fibers exhibited a main endothermic peak at 284 °C, attributing to the thermal decomposition of a *β*-sheet crystalline. Adding CNC, the endothermic peak shifted to slightly higher temperature, but the peak locations remained nearly unchanged until 7 wt % CNC content, which implied that CNC could affect the thermal degradation of SF molecules. In the case of natural silk fibers, degummed silks displayed higher endothermic peaks at 315 °C.

To obtain more information on thermal decomposition behavior, TGA measurement was performed on degummed silk and various CNC/SF fibers, as shown in Fig. 8. CNC (Fig. S2c) and degummed silk showed 0.2% and 14.5% of residual weight at 700 °C, respectively. It was expected that the residual weight percent of CNC/SF fibers at 700 °C increased with increasing CNC contents except 5 wt% of CNC. However, a large difference between degummed silk and CNC/SF fibers was the maximum decomposition temperature (T_{max}), known as a criterion of thermal decomposition. This unique phenomenon could be displayed clearly in a differential TGA (DTG) curves as shown in Fig. 8b. The degummed silk exhibited a T_{max} at around 350 °C, much higher than that of regenerated SF fibers by about 20 °C (Table 1). However, compared with regenerated SF fibers, T_{max} of CNC/SF fibers improved sharply at first and then decreased slightly with the increase of CNC contents. These results reconfirmed that the thermal degradation and thermal stability were affected by adding CNC, consisting with the result of DSC. In addition, it was worth noting that two T_{max}s appeared at 329 °C and 368 °C when the CNC content reached 7 wt%. The former was corresponded to the decomposition of SF, the later was related to the decomposition of CNC. The thermal decomposition behavior of CNC/SF fibers could be summarized as the following two features.

One is that the T_{max} of CNC/SF fibers maximized to 344 °C when 3 wt% of CNC was added, and then decreased with further increasing CNC contents. It was well confirmed that the cellulose nanocrystals by the sulfuric acid hydrolysis exhibited two degradation stages, i.e. a lower temperature stage and a higher temperature stage

resulting from residual sulfated anhydroglucose units.[52,53] In this work, Lower initial decomposition temperature at 216 ℃ and broader degradation range were detected, as shown in Fig. S2d. A shoulder peak at 370 ℃ and a main decomposition peak at 567 ℃ appeared, suggesting there are two degradation stages. The lower temperature stage was related to the degradation of more accessible and more highly sulfated amorphous regions, whereas the higher temperature stage is related to the breakdown of unsulfated crystal interior.[42,53] Therefore, the thermal decomposition behavior of CNC/SF fibers can be explained that the molecular interactions between SF and CNC restrained the decomposition of SF, consequently improving the thermal stability of CNC/SF fibers. When the CNC content was increased more than 3 wt%, the release of sulfuric acid group in residual sulfated anhydroglucose units in CNC accelerated the decomposition of SF, as a result, poor thermal stability of SF occurred.[54,55] The other feature is that the two T_ms are present in CNC/SF fiber with 7 wt% CNC. This implies that the accelerating action of CNC on the SF is not strong in this blend ratio. However, it seems that there was still accelerating action of SF when considering T_m of SF was changed from 330 to 329 ℃. Those two features might be due to the following two effects: 1) molecular interactions between SF and CNC during the thermal decomposition process and 2) accelerating effect on the decomposition between the polymers.

3.5 Dynamic mechanical transitions

Dynamic loss tangent (tanδ) curves of DMA are widely used to explain molecular movement of polymers and the resulted structure changes. Typical DMA results of degummed silk and CNC/SF fibers (3X) were shown in Fig. 9. The storage modulus

(lg E') value remained almost constant as the temperature increased up to 180 °C, and then decreased rapidly as a result of thermal relaxation of fibroin backbone. And the descent rate of CNC/SF fibers was faster than that of degummed silk, indicating different thermal relaxation behavior. Correspondingly, the tanδ curve showed little change until at 180 °C where the tanδ peak began to appear and reached a maximum. This temperature of tanδ peak was taken as the glass transition temperature (Tg) of amorphous regenerated fibers. Using data from DMA curves, we then analyzed CNC/SF fibers' segmental movements via different CNC contents.

It was found that CNC has a reinforcing effect on the CNC/SF fibers modulus as shown in Fig. 9. Compared with the regenerated SF fiber, the modulus was substantially increased with the increase of CNC in the CNC/SF fibers, which might be attributed to the formation of a rigid nanocrystal network governed by a percolation mechanism within the host matrix.[54] Fig. 9b and Table 1 showed the T_g values during the relaxation process associated with the viscoelastic manifestation of the glass-rubber transition of the amorphous regions in the CNC/SF fibers. In the case of the regenerated SF fiber, the T_g appeared at 225 °C and shifted to high temperature with the increase of CNC contents, suggesting a reduced mobility of amorphous SF chains in the presence of interactions between the CNC and the matrix, consisting with the FTIR spectra. On the other hand, the amplitude of tanδ peak at T_g decreased with the increase of CNC content, which may be ascribed to the decrease of mobile units of SF participating in the relaxation process.

In our previous report on CNC/SF composite films using PEG as a plasticizer,

either storage modulus or tanδ peaks of CNC/SF composite films were all lower than those of CNC/SF fibers,[56] indicating the difference of molecular structure. Among the regenerated CNC/SF fibers and films, considering that they have nearly equal molecular weights and composition, dynamic mechanical transitions may be affected by crystallization and molecular orientation. Thermal relaxation of *β*-sheet domains of silk fibroin should appear at a higher temperature (i.e. above 200 °C).[57] Therefore, the tanδ peak of CNC/SF films ranged from 178.4 °C -190.8 °C should be related to the relaxation of permanently disordered domains of silk fibroin with more free motility (vs. *β*-sheet domains). However, in the case of CNC/SF fibers, the local motility of disordered domains was limited by the hydrogen bonds between CNC and SF. Furthermore, in wet spinning process, highly concentrated dope-facilitated and methanol-induced *β*-sheet crystallization as well as draw-induced orientation occurred, therefore more ordered structure in CNC/SF fibers might increase the T_g of disordered domains, which was consistent with the results obtained from the XRD and thermal degradation.

3.6 Mechanical properties

Stress–strain curves of degummed silk and CNC/SF fibers (3X) were shown in Fig. 10. In the case of draw ratio of 1X and 2X was shown in Fig. S3. Regardless of CNC content, the breaking stress increased, whereas the breaking strain decreased as the draw ratio increased. On the whole, the breaking stress of CNC/SF fibers was in the range of 185-750 MPa and breaking strain 18%-40% depending on the draw ratio. And the breaking stress and strain of CNC/SF (3X) were significantly greater than those of the degummed silk, though the tensile properties of regenerated SF fiber

approached that of the degummed silk, which were 477.1 MPa of stress and 19.7% of breaking strain. The reinforcing of CNC on the tensile properties of CNC/SF fibers was clear. The specific stress increased persistently with CNC contents.

Fig.11 presented the effect of CNC on the tensile strength and Young's modulus of CNC/SF fibers drawn at different ratios. It was clearly observed that with the increase of the draw rate and CNC contents, the CNC/SF fibers exhibited a drastic improvement in tensile strength and Young's modulus. When the CNC content increased to 5 wt% in CNC/SF fibers (3X), the tensile strength and Young's modulus were increased up to maximum of 728.5±36.4 MPa and 28.8±2.6 GPa, respectively followed with a decrease to 692.2±29.6 MPa and 25.0±2.5 GPa when the CNC content was 7 wt%. In this paper, the tensile strength, Young's modulus and breaking strain of degummed silk were 477.1±6.5 MPa, 16.3±3.7 GPa and 19.7±1.45, respectively. Thus, it was affirmed that CNC exhibited a noteworthy reinforcing effect. This improvement could be attributed to two aspects: the movement of the molecular chain in the ordered amorphous region, while the molecular chain in the disordered amorphous region was restrained during the deformation because of hydrogen bonding interaction between CNC and SF. On the other hand, the refined crystalline structure and orientation of SF formed after the addition of CNCs with large aspect ratio, high degree of crystallinity.

4. Conclusion

The continuous CNC/SF fibers with an ordered crystalline structure and molecular orientation were successfully produced by incorporating CNC into SF matrix to mimic the β-sheet crystallite in natural silk. We have demonstrated that rod-like CNC

uniformly dispersed into SF matrix and formed intermolecular hydrogen bonding interactions in disordered amorphous region of SF, resulting in the ordered amorphous region combining with the post-draw, simultaneously, CNC facilitated the crystallization of SF molecules. As a result, improvements on the thermal stability and mechanical properties of the CNC/SF fibers were obtained. Compared with pure SF fiber, the Young's modulus, tensile strength and breaking strain of the CNC/SF fibers were improved by 195%, 160% and 130%, respectively. This study will provide a new promising strategy to design high performance biomimic silk as well as broaden the potential use of such artificial animal silk.

Acknowledgements

The work is financially supported by the National Science Foundation of China (51303159, 51172207), National Science Foundation of Zhejiang Province (LQ13E030008), Research Fund for the Doctoral Program of Higher Education of China (20103318110001, 20123318120004), Program for Zhejiang Leading Team of Science and Technology Innovation (2011R50003) and Program for Zhejiang Top Priority Discipline of Textile Science and Engineering (2013YXQN06, 101819-Y).

References

1 F. G. Omenetto and D. L. Kaplan, *Science*, 2010, **329**, 528-531.

2 C. Muller, M. Hamedi, R. Karlsson, R. Jansson, R. Marcilla, M. Hedhammar and O. Inganas, *Adv. Mater.*, 2011, **23**, 898-901.

3. G. Q. Liu, X. P. Huang, Y. J. Wang, Y. Q. Zhang and X. W. Wang, *Soft Matter*, 2012, **8**, 9792-9799.

4 K. Zhang, F. W. Si, H. L. Duan and J. Wang, *Acta Biomater.*, 2010, **6**, 2165-2171.

5 B. B. Mandal and S. C. Kundu, *Acta Biomater.*, 2010, **6**, 360-371.

6 L. P. Yan, J. M. Oliveira, A. L. Oliveira, S. G. Caridade, J. F. Mano and R. L. Reis, *Acta Biomater.*, 2012, **8**, 289-301.

7 R. E. Unger, S. Ghanaati, C. Orth, A. Sartoris, M. Barbeck, S. Halstenberg, A. Motta, C. Migliaresi and C. J. Kirkpatrick, *Biomaterials*, 2010, **31**, 6959-6967.

8 A. S. Lammel, X. Hu, S. H. Park, D. L. Kaplan and T. R. Scheibel, *Biomaterials*, 2010, **31**, 4583-4591.

9 H. J. Jin and D. L. Kaplan, *Nature*, 2003, **424**, 1057-1061.

10 Y. X. He, N. N. Zhang, W. F. Li, N. Jia, B. Y. Chen, K. Zhou, J. H. Zhang, Y. X. Chen and C. Z. Zhou, *J. Mol. Biol.*, 2012, **418**, 197-207.

11 Y. Suzuki, J. T. Gerig and T. Asakura, *Macromolecules*, 2010, **43**, 2364-2370.

12 Y. Suzuki, A. Aoki, Y. Nakazawa, D. P. Knight and T. Asakura, *Macromolecules*, 2010, **43**, 9434-9440.

13 M. Cetinkaya, S. Xiao and F. Grater. *Soft Matter*, 2011, **7**, 8142-8148.

14 M. S. Creager, J. E. Jenkins, L. A. Thagard-Yeaman, A. E. Brooks, J. A. Jones, R. V. Lewis, G. P. Holland and J. L. Yarger, *Biomacromolecules*, 2010, *11*, 2039-2043.

15 Q. Q. Dang, S. D. Lu, S. Yu, P. C. Sun and Z. Yuan, *Biomacromolecules*, 2010, **11**, 1796-1801.

16 C. H. Zhao, J. M. Yao, H. Masuda, R. Kishore and T. Asakura, *Biopolymers*, 2003, **69**, 253-259.

17 J. M. Yao, H. Masuda, C. H. Zhao and T. Asakura, *Macromolecules*, 2002, 35, 6-9.

18 S. W. Ha, A. E. Tonelli and S. M. Hudson, *Biomacromolecules*, 2005, **6**, 1722-1731.

19 I.C. Um, C.S. Ki, H.Y. Kweon, K.G. Lee, D.W. Ihm and Y.H. Park, *Int. J. Biol. Macromol.*, 2004, **34**, 107–119.

20 E. Marsano, P. Corsini, C. Arosio, A. Boschi, M. Mormino and G. Freddi, *Int. J. Biol. Macromol.*, 2005, **37**, 179-188.

21 D.M. Phillips, L. F. Drummy, R. R. Naik, H. C. De Long, D. M. Fox, P. C. Trulove and R. A. Mantz, *J. Mater. Chem.*, 2005, **15**, 4206-4208.

22 G. Q. Zhou, Z. Z. Shao, D. P. Knight, J. P. Yan and X. Chen, *Adv. Mater.*, 2009, **21**, 366-370.

23 J. P. Yan, G. Q. Zhou, D. P. Knight, Z. Z. Shao and X. Chen, *Biomacromolecules*, 2010, **11**, 1-5.

24 Z. H. Zhu, T. Imada and T. Asakura, *Mater. Chem. Phys.*, 2009, **17**, 430-433.

25 H. Pan, Y. P. Zhang, Y. C. Hang, H. L. Shao, X. C. Hu, Y. M. Xu and C. Feng, *Biomacromolecules*, 2012, **13**, 2859-2867.

26 F. Zhang, B. Q. Zuo, Z. H. Fan, Z. G. Xie, Q. Lu, X. G. Zhang and D. L. Kaplan, *Biomacromolecules*, 2012, **13**, 798-804.

27 C. R. Wittmer, T. Claudepierre, M. Reber, P. Wiedemann, J. A. Garlich, D. Kaplan, C. Egles, *Adv. Fun. Mater.*, 2011, **2**1, 4232-4242.

28 A. J. Meinel, K. E. Kubow, E. Klotzsch, M. Garcia-Fuentes, M. L. Smith, V. Vogel, H. P. Merkle and L. Meinel, *Biomaterials*, 2009, **30**, 3058-3067.

29 A. Schneider, X. Y. Wang, D. L. Kaplan, J. A. Garlick and C. Egles, *Acta Biomaterialia*, 2009, **5**, 2570-2578.

30 A. Martel, M. Burghammer, R. J. Davies, E. D. Cola, C. Vendrely and C. Riekel, *J. Am. Chem. Soc.*, 2008, **130**, 17070-17074.

31 P. Domachuk, K. Tsioris, F. G. Omenetto and D. L. Kaplan, *Adv. Mater.*, 2010, **22**, 249-260.

32 J. Luo, Y. P. Zhang, Y. Huang, H. L. Shao and X. H. Hu, *Sens. Actuators B: Chemical*, 2012, **162**, 435-440.

33 M. E. Kinahan, E. Filippidi, S. Koster, X. Hu, H. M. Evans, T. Pfohl, D. L. Kaplan and J. Wong, *Biomacromolecules*, 2011, **12**, 1504-1511.

34 S. K. Chae, E. Kang, A. Khademhosseini and S. H. Lee, *Adv. Mater.*, 2013, **25**, 3071-3078.

35 Z. Z. Shao and F. Vollrath, *Nature*, 2002, **48**, 741.

36 T. P. Knowles, A. W. Fitzpatrick, S. Meehan, H. R. Mott, M. Vendruscolo, C. M. Dobson and M. E. Welland, *Science*, 2007, **318**, 1900-1903.

37 W. G. Qiu, W. B. Teng, J. Cappello and X. Y. Wu, *Biomacromolecules*, 2009, **10**, 602-608.

38 N. Lin, J. Huang and A. Dufresne, *Nanoscal*, 2012, **4**, 3274-3294.

39 Y. Habibi, S. Aouadi, J. M. Raquez and P. Dubois, *Cellulose*, 2013, **20**, 2877-2885.

40 N. Lin and A. Dufresne, *Macromolecules*, 2013, **46**, 5570-5583.

41 J. M. Raquez, Y. Murena, A. L. Goffin, Y. Habibi, B. Ruelle, F. DeBuyl and P. Dubois, *Compos. Sci. Technol.*, 2012, **72**, 544-549.

42 S. H. Park, K. W. Oh and S. H. Kim, *Compos. Sci. Technol.*, 2013, **86**, 82-88.

43 X. D. Wu, C. H. Lu, W. Zhang, G. P. Yuan, R. Xiong and X. X. Zhang, *J. Mater. Chem*. A, 2013, **1**, 8645-8652.

44 R. J. Li, J. M. Fei, Y. R. Cai, Y. F. Li, J. Q. Fei and J. M. Yao, *Carbohyd. Polym.*, 2009, **76**, 94-99.

45 J. T. Wang, L. L. Li, L. Feng, J. F. Li, L. H. Jiang and Q. Shen, *Int. J. Biol. Macromol*., 2014, **63**, 205-209.

46 M. J. Sun, Y. P. Zhang, Y. M. Zhao, H. L. Shao and X. C. Hu, *J. Mater. Chem.*, 2012, **22**, 18372-18379.

47 L. Liu and J. M. Yao, *Adv. Mater. Res.*, 2011, **175-176**, 272-275.

48 N. Hameed, Q. Guo, F.H. Tay and S.G. Kazarian, *Carbohydr. Polym.,* 2011, **86**, 94-104.

49 H. Y. Yu, Z. Y. Qin, L. Liu, X. G. Yang, Y. Zhou and J. M. Yao, *Compos. Sci. Technol*., 2013, **87**, 22-28.

50 W.W. Moseley Jr, *J. Appl. Polymer Sci*, 1960, **3**, 266-276.

51 K. J. Koski, P. Akhenblit, K. Mckiernan and J. L. Yarger, *Nat. Mater.*, 2013, **12**, 262-267.

52 E. De M. Teixeira, A. C. Corrêa, A. Manzoli, F. De L. Leite, C. R. De Oliveira and L. H. C. Mattoso, *Cellulose*, 2010, **17**, 595-606.

53 M. F. Rosa, E. S. Medeiros, J. A. Malmonge, K. S. Gregorski, D. F, Wood, L. H. C. Mattoso, G. Glenn, W. J. Orts and S. H. Imam, *Carbohyd. Polym.*, 2010, **81** 83-92.

54 E. Ten, J. Turtle, D. Bahr, L. Jiang and M. Wolcott, *Polymer*, 2010, **51**, 2652-2660.

55 H. Y. Yu, Z. Y. Qin, B. L. Liang, N. Liu, Z. Zhou and L. Chen, *J. Mater. Chem. A,* 2013, **1**, 3938-3944.

56 R. J. Li, Y. H. Zhang, L. J. Zhu and J. M. Yao, *J. Appl. Polym. Sci.*, 2012, **124**, 2080-2086.

57 Q. Q. Yuan, J. R. Yao, L. Huang, X. Chen and Z. Z. Shao, *Polymer*, 2010, **51**, 6278-6283.

Table 1 Hydrogen bond fractions ($F_{H\text{-}CO}$) and thermal analysis parameters for degummed silk, regenerated SF fiber and CNC/SF fibers with various CNC contents.

Samples	Degummed silk	SF fiber	1%CNC/SF	3%CNC/SF	5%CNC/SF	7%CNC/SF
$F_{H\text{-}CO}$	/	/	0.50	0.51	0.54	0.60
T_{endo}(℃) [a]	315	284	286	286	285	289
T_{max}(℃)	350	330	342	344	329	329/368
T_g(℃)	225	225	228	227	234	236

a T_{endo} was main endothermic peak temperature obtained from the DSC curves.

Figure captions:

Fig. 1. Illustration of the formation of self-aggregated fibers: Scheme of silkworm spinning (a). Scheme of biomimic silk fiber via cellulose nanocrystal as β-sheet crystallite (b).

Fig. 2. SEM image of surface and cross section morphologies of CNC/SF fiber with 7 wt% CNC (a), FE-SEM images of cross section morphologies of SF fiber (b) and CNC/SF fibers with CNC 1wt% (c), 3wt% (d), 5wt% (e) and 7 wt% (f).

Fig. 3. FTIR spectra (a) of degummed silk (A), SF fiber (B), and CNC/SF fibers with CNC 1wt% (C), 3wt% (D), 5wt% (E) and 7 wt% (F), and fitting-curve of the carbonyl band of CNC/SF fiber with 7 wt% CNC (b).

Fig. 4. XRD patterns (a) and crystallinity (b) of degummed silk and regenerated SF fibers with different draw ratio.

Fig. 5. XRD patterns (a) and crystallinity (b) of regenerated SF fibers and CNC/SF fibers with different CNC contents.

Fig. 6. Sound velocity of regenerated SF fibers and various CNC/SF fibers with different draw ratio.

Fig. 7. DSC thermograms of degummed silk (A), SF fiber (B), and CNC/SF fibers with CNC 1wt% (C), 3wt% (D), 5wt% (E) and 7 wt% (F).

Fig. 8. TGA and DTG thermograms of degummed silk, regenerated SF fibers and CNC/SF fibers with different CNC contents.

Fig. 9. Storage modulus (a) and tanδ curves of degummed silk, regenerated SF fibers and CNC/SF fibers with different CNC contents.

Fig. 10. Stress-strain curves of degummed silk, regenerated SF fibers and CNC/SF fibers with different CNC contents.

Fig. 11. Young's modulus (a) and tensile strength of degummed silk, regenerated SF fibers and various CNC/SF fibers with different draw ratio

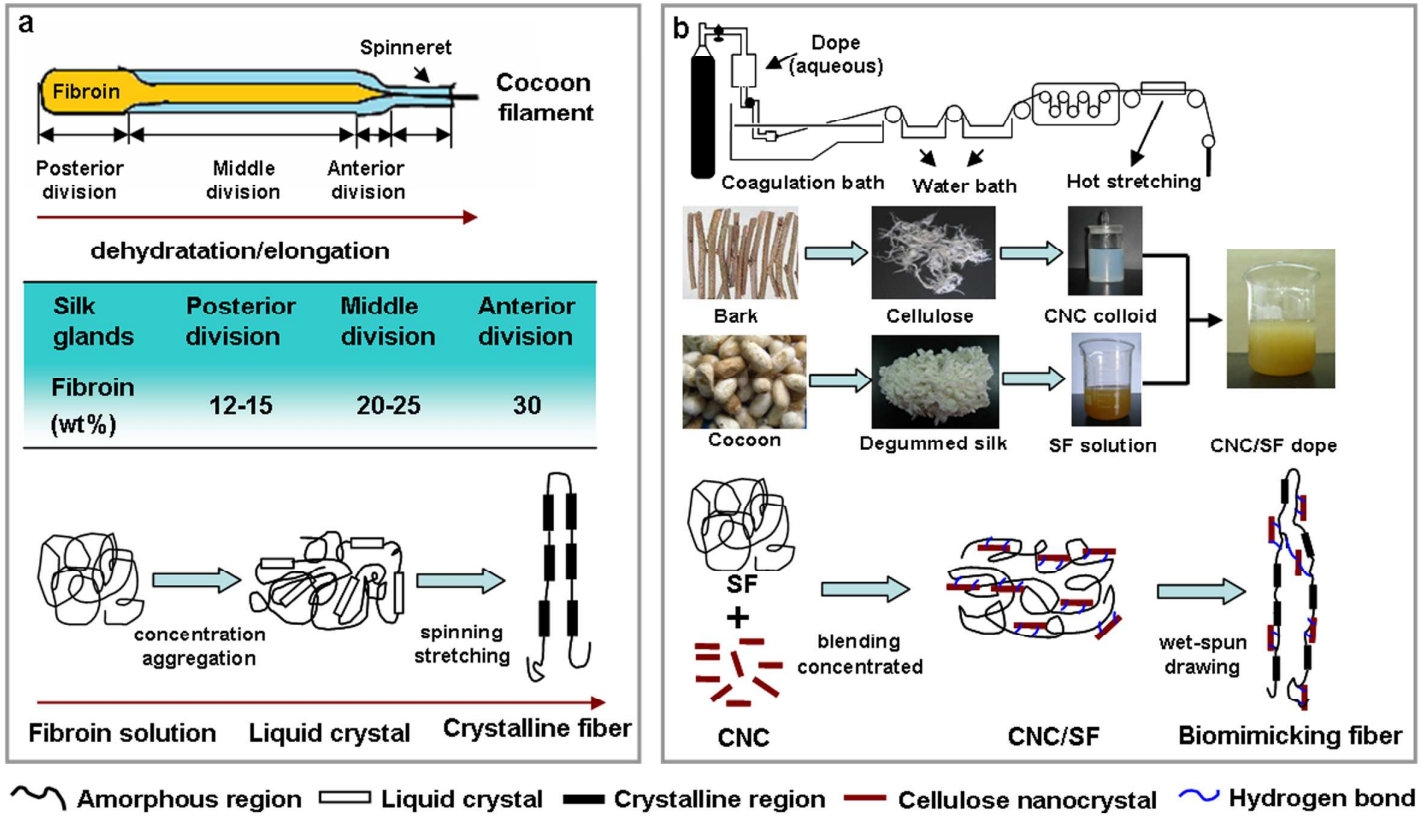

Fig. 1

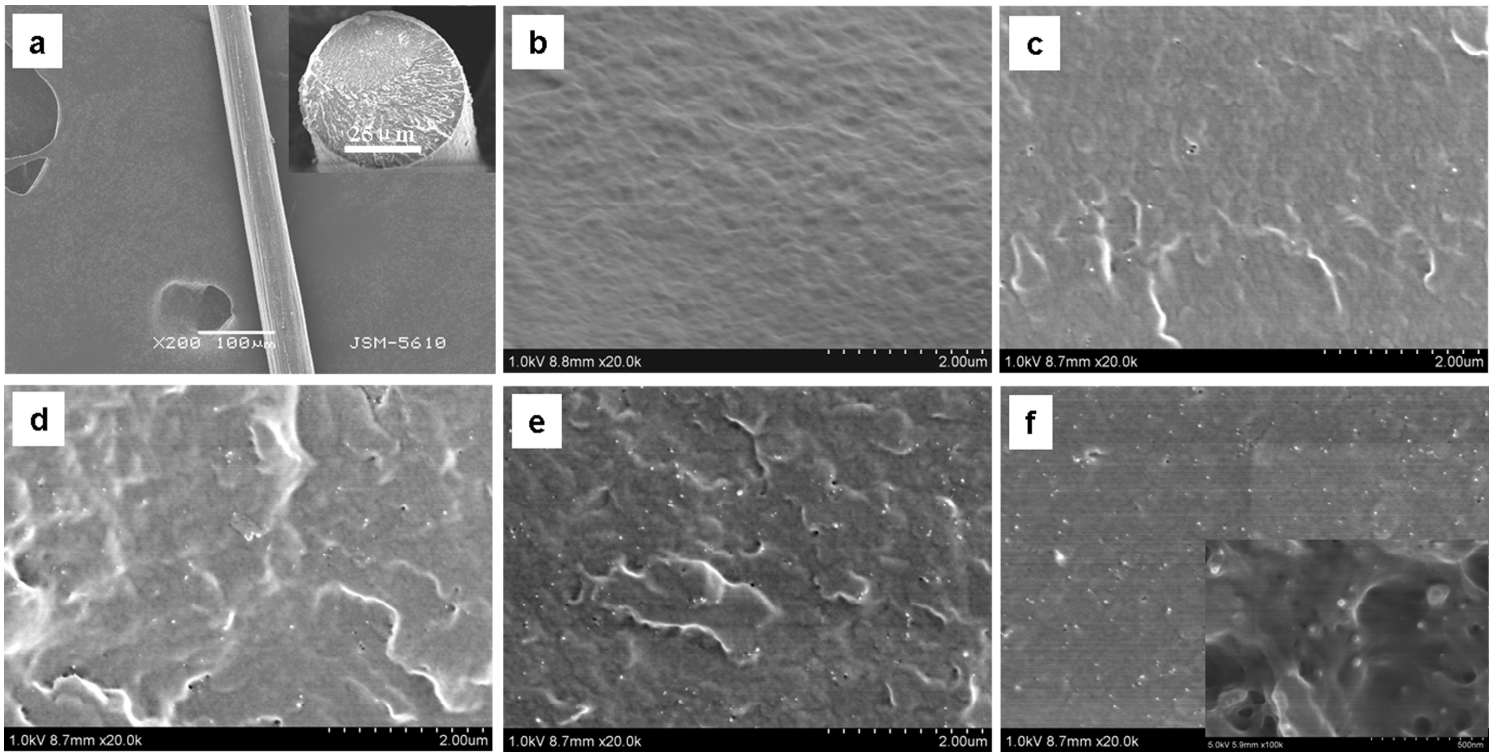

Fig. 2

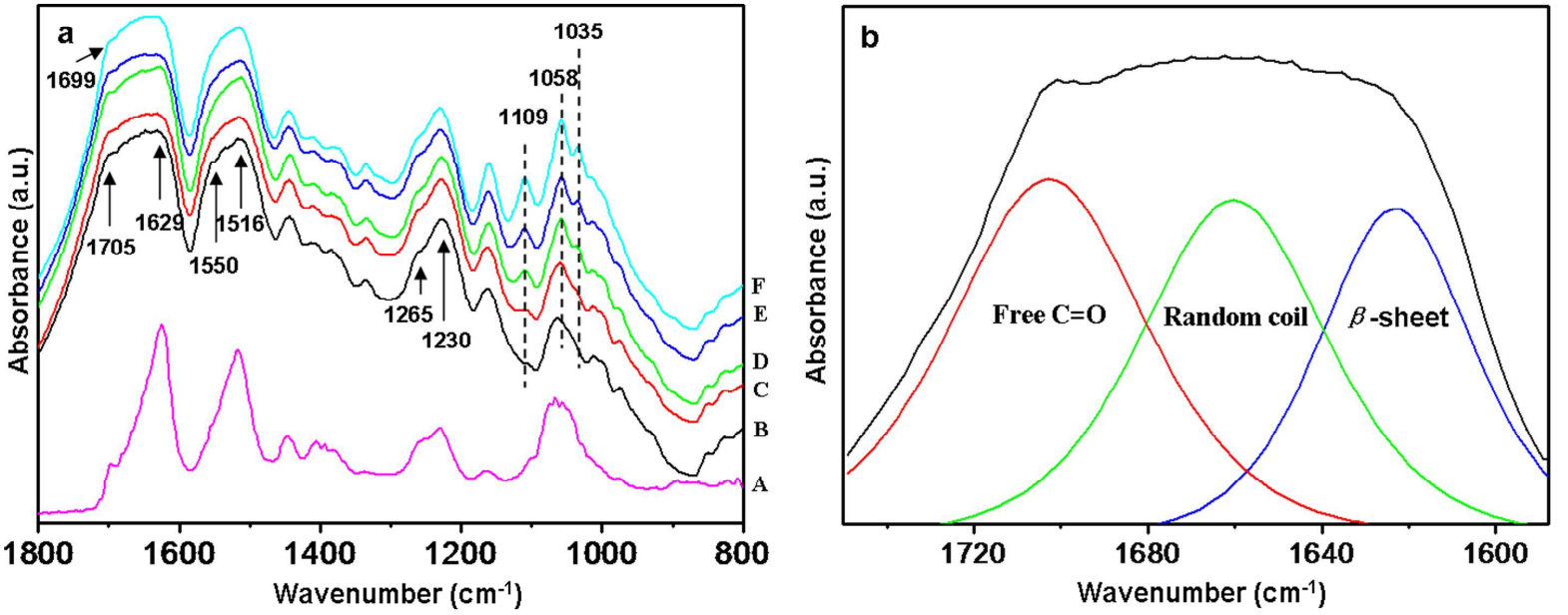

Fig.3

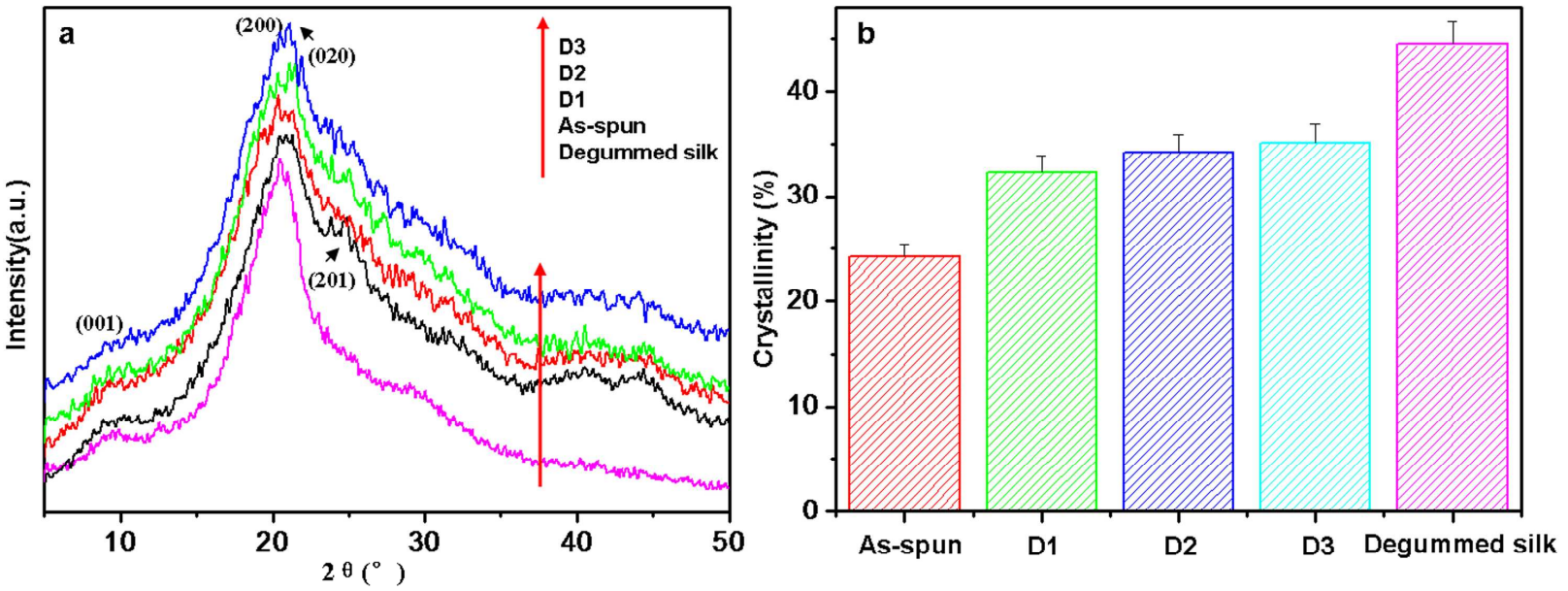

Fig. 4

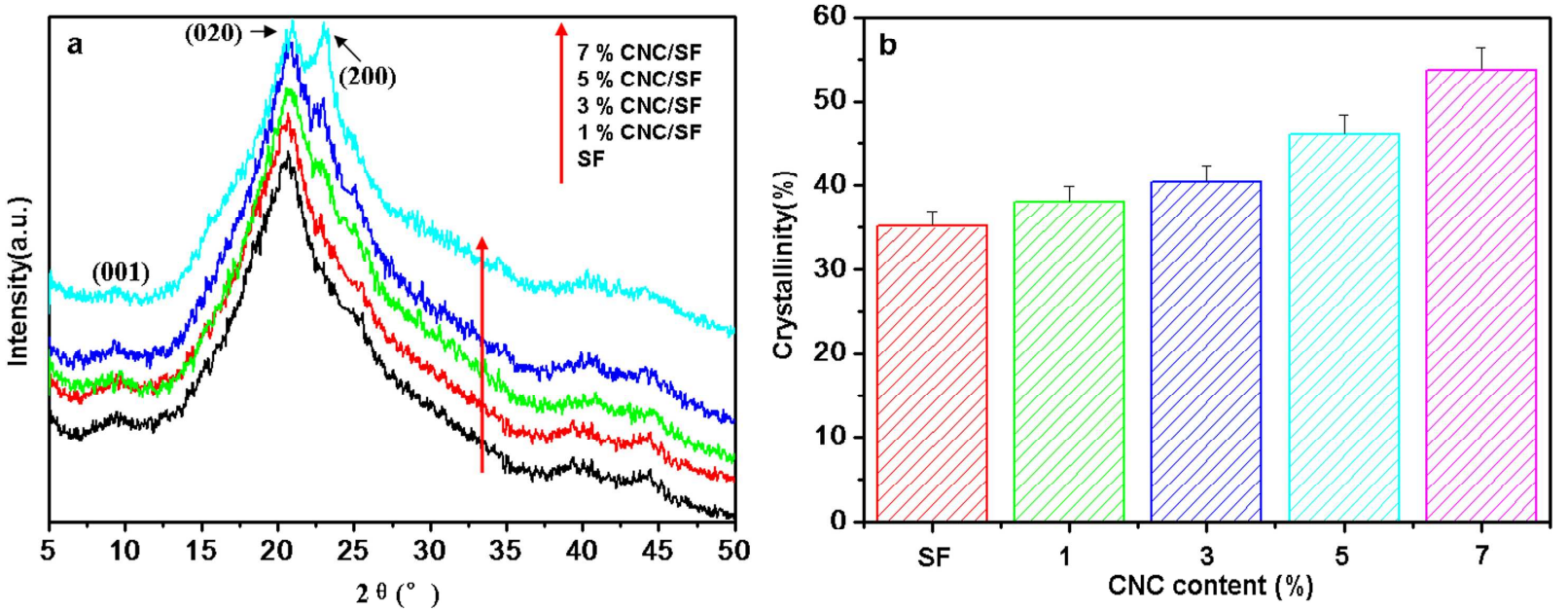

Fig. 5

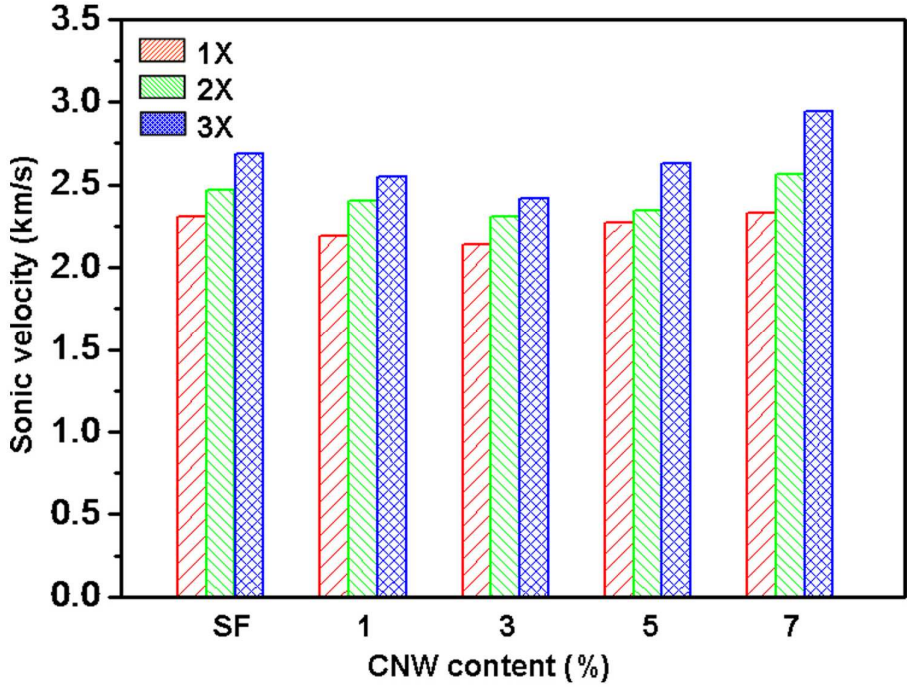

Fig. 6

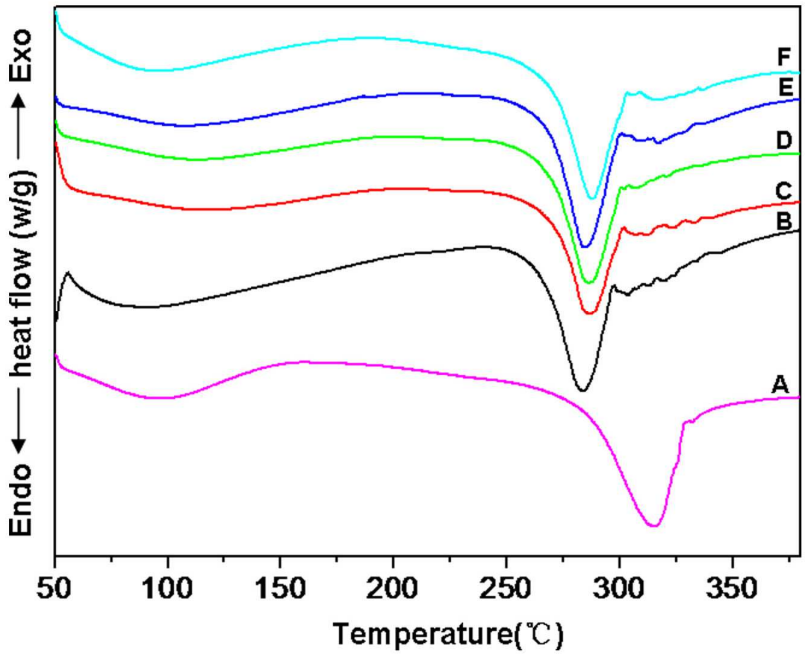

Fig. 7

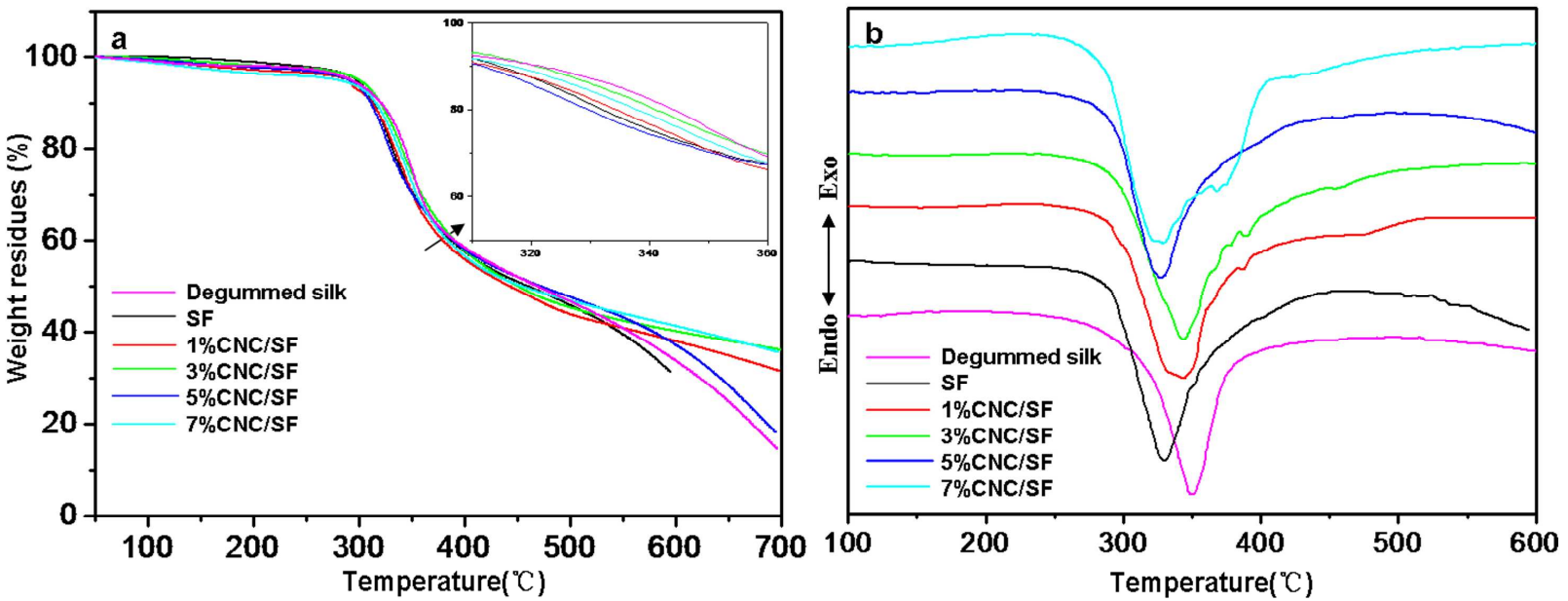

Fig. 8

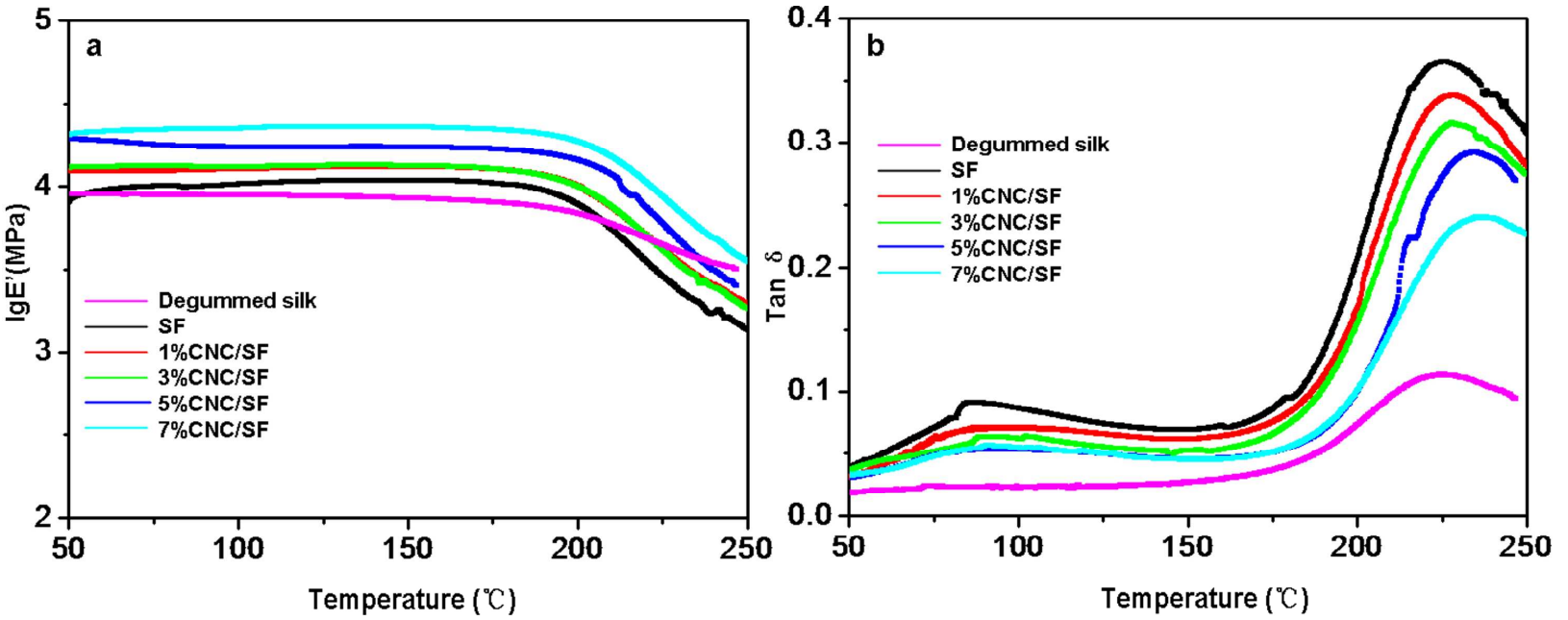

Fig. 9

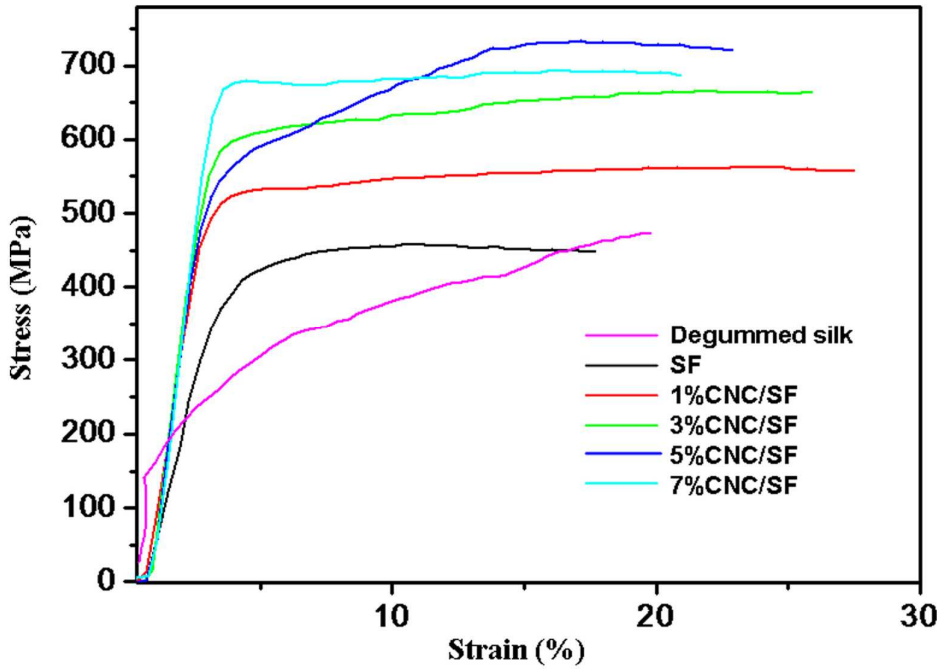

Fig. 10

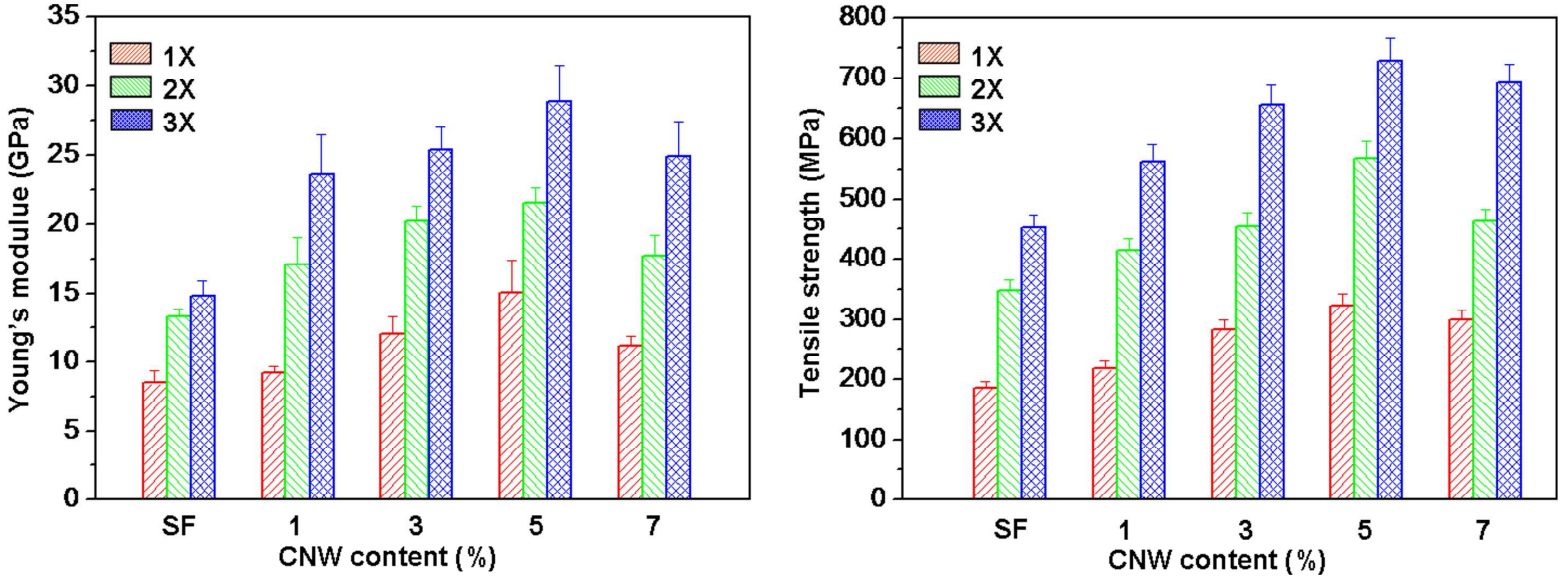

Fig. 11